IET The Institution of Engineering and Technology WILEY

ORIGINAL RESEARCH

Reversible hybrid control resonant converter for electric vehicle battery charging and discharging system

Jeng-Yue Chen[1] 🆔 | Sin-Yan Wu[1] | Gwo-Jen Chiou[1] | Fuh-Shyang Juang[2]

[1]Department of Electrical Engineering, National Formosa University, Huwei, Yunlin, Taiwan

[2]Department of Electro-Optical Engineering, National Formosa University, Huwei, Yunlin, Taiwan

Correspondence
Jeng-Yue Chen, Department of Electrical Engineering, National Formosa University, 64 Wunhua Road, Huwei, Yunlin 63208, Taiwan.
Email: buo@nfu.edu.tw

Abstract
In this study, the control modes in the newly designed converter include a variable frequency control mode, a phase shift control mode, and hybrid switching with a dual control mode. Compared with the traditional resonant converter, the newly designed converter has the following characteristics: (1) Zero voltage and zero current soft switching to improve converter efficiency in forward and reverse mode and wide voltage range, (2) solves the problem of voltage adjustment being difficult and switching loss increasing at light load for the resonant converter under the variable frequency control mode, (3) hybrid switching with a dual-control strategy to resolve the design difficulty of digital control in hybrid switching control mode, (4) a closed loop control for the resonant converter with hybrid switching and dual-control mode. Finally, In the forward charging mode, the input voltage is 400 V, the output voltage is 250–450 V, the maximum power is 1000 W, and the maximum efficiency is 96.69%. In reverse discharge mode, the input voltage is 250–450 V, the output voltage is 400 V, and the efficiency at full load is 95.13%. The maximum conversion efficiency is 97.57% when the output power is 840 W.

JEL CLASSIFICATION
Power electronics, electric power applications

1 | INTRODUCTION

Due to policy promotion, the market share of new energy vehicles has increased year by year recently. To solve the phenomenon that green energy cannot generate electricity in time during the peak period of electricity consumption, the charging and discharging concepts of Grid-to-Vehicle (G2V) and Vehicle-to-Grid (V2G) are proposed in [1–3]. The high-voltage battery pack of electric vehicles as a distributed energy storage system was employed to solve the problem of electric energy storage [4–6]. Therefore, the energy storage system of electric vehicles must have the function of bidirectional electrical energy conversion.

The architecture of bidirectional DC–DC converter can be divided into isolated and non-isolated type. Among them, the research and application for isolated type are more popular. In term of power level and control freedom, most of the medium and high-power applications adopt the full-bridge architecture.

In isolated bidirectional DC–DC converter applications, the Dual Active Phase-shift Full-bridge converter (DAB) belongs to zero voltage switching (ZVS) architecture, which is the most widely used and most representative architecture [7–8]. But the converter has some problems in actual applications. For example, the conditions to achieve ZVS soft switching are different respectively for leading leg switch and lagging leg switch, on the primary side of H bridge. It is common for phase-shifted full-bridge converters that the lagging leg switch causes duty-cycle loss and soft-switching failure during operation. And at light load, the circulating current in resonant circuit decreases and the ZVS range of the converter reduces. So, it is difficult to realize the soft switching of the converter over all loading [9–11]. Therefore, resonant technology has always been the focus of research on soft switching of switches [12–13]. Based on a dual active phase-shift full-bridge converter, the serial resonant converter (SRC) is composed of a capacitor connected with series inductor on the primary side of the transformer.

For AC components at different frequencies, SRC presents different impedances. When the switching frequency is higher than the resonant frequency, the input impedance is inductive, and the primary-side switch can realize the ZVS soft-switching characteristics. While the switching frequency is lower than the resonant frequency, the input impedance is capacitive, and the primary-side switch can realize the zero-current switching (ZCS) soft-switching characteristics. But this scheme is not suitable for applications in wide input or output voltage range because of their different soft-switching characteristics of the forward and reverse working states that will increase the control complexity [14]. In addition, if the magnetizing inductance of the transformer is taken into consideration, the magnetizing inductance is connected in series with the resonant inductance and resonant capacitor to form a LLC resonant converter. In the reverse mode, the entire converter is similar to a series resonant converter. Only buck and ZVS or ZCS soft switching can be achieved on the secondary side [15–18]. In order to improve the weakness of traditional bidirectional resonant converters, the resonant inductors and resonant capacitors are added in the secondary side to form a full-bridge CLLLC resonant converter, which simplifies the complexity of the control method during forward and reverse operation period. The converter can achieve buck-boost and soft-switching characteristics during forward and reverse operation mode [19].

To ensure uniform characteristics for bidirectional operation, the secondary LC resonant tank components are usually designed to be equal to the primary LC components after reflection. However, for reducing the bidirectional frequency range variation, the detailed asymmetric parameters methodology (APM) is proposed to address undesirable large switching frequency range. It can design gain curves for charging and discharging modes separately, thereby result in lower switching loss caused by excessive high frequency [20]. To address the difficulty of symmetric/asymmetric parameter design, a bidirectional unified modelling, analysis, and design method is proposed [21–22]. By selecting appropriate and quantitative bidirectional circuit factors, this model unifies the forward and reverse circuits which greatly simplifies the calculation or iteration of the parameter design and the complexity of bidirectional synchronous rectification (SR) [23]. To further improve the efficiency, the synchronous rectification (SR) control is introduced by controlling the turn-on and turn-off timings based on the phase difference between primary gate pulse and secondary resonant current [24]. And the novel extended harmonics approximation (EHA) modelling approach is introduced for CLLC resonant converters to estimate the phase of its secondary side current accurately [25]. And then the dynamic nature of CLLLC-type bidirectional resonant converter is highly dependent on loading conditions, which proves challenging when designing the voltage and current closed-loop controllers. So, the design methodology of Extended Describing Functions (EDF) is proposed to focus on defining the worst operating scenarios for the converter [26]. In addition to improve the analysis and design of converter, the phase shift control was proposed to reduce the output voltage ripple of resonant converter, which also has a faster transient response for output voltage in

the hybrid control mode [27], and effectively suppress the voltage and current surges at start-up [28]. To reduce the variable frequency control range in wide voltage applications, the variable frequency and phase shift control mode are combined and proposed. When the switching frequency is greater than the resonant frequency, the phase shift modulation is added. But the switching processes of its control mode are not smooth [29, 30].

For the second-stage DC–DC converter of the two-stage electric vehicle charger [3, 5], a symmetric full-bridge CLLLC resonant converter for charging and discharging batteries is proposed. Compared with variable frequency control of traditional bidirectional DC–DC converter, in this study the hybrid switching with dual control strategy was employed to achieve zero voltage and zero current switching of bidirectional buck and boost mode. The conventional variable-frequency control cannot achieve zero current switching for the rectifier at buck mode. The dual control strategy in this study can avoid the increase of switching loss at high frequency, and thus improve the converter efficiency. The ideal hybrid switching model is only suitable for traditional open loop control. This study proposes a dual control strategy with hybrid switching to achieve closed loop control, which combines both variable frequency and phase-shift control in the strategy and can thus achieve bidirectional, wide-voltage, and full-range soft-switching functions.

2 | FUNDAMENTAL ANALYSIS

2.1 | Converter power stage

The circuit architecture of the full-bridge CLLLC resonant converter is shown in Figure 1. S_1–S_4 and S_5–S_6 are power switches of the inverter and rectifier circuit on each side of the transformer, respectively. L_{r1} and L_{r2} are resonant inductors including the leakage inductance of the transformer, C_{r1} and C_{r2} are the resonant capacitors, L_m is the transformer magnetizing inductance, C_{oss1}–C_{oss8} are parasitic capacitances on the power switch, and C_1 and C_2 are filter capacitors.

The converter can be divided into three parts: Inverter circuit, resonant circuit and rectifier circuit. The power switches convert the DC voltage to AC square wave. The AC square voltage enters the resonant circuit, passes through the transformer, the rectifier circuit and is filtered by the filter capacitor. A stable DC voltage is generated. The output energy is adjusted by changing the working frequency and phase angle difference between power switches S_1–S_4. And this study defines the energy transfer from V_1 to V_2 as for-ward battery charging mode (FBCM) and V_2 to V_1 as reverse battery discharge mode (RBDM). R_L is the load.

2.2 | Operation of variable frequency control

In this study, the full-bridge CLLLC converter is theoretically analyzed with symmetrical parameters. Firstly, the variable frequency control strategy commonly used in resonant converters
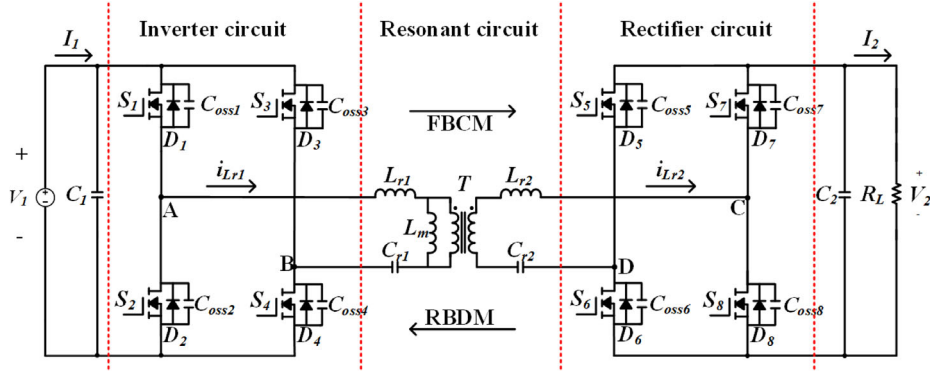
FIGURE 1 CLLLC resonant converter designed in this study

is used. Taking FBCM as an example, the converter working frequency is divided into the resonant frequency f_r, second resonant frequency f_m and switch frequency f_s. f_r and f_m are defined as Equations (1) and (2), respectively.

$$f_r = \frac{1}{2\pi\sqrt{L_{r1}C_{r1}}} \tag{1}$$

$$f_m = \frac{1}{2\pi\sqrt{(L_{r1} + L_m)C_{r1}}} \tag{2}$$

The working mode of the converter designed in this study is the boost mode in which the magnetizing inductance participates in resonance at forward and reverse operation frequencies. Therefore, the following analysis is carried out for this interval:

1. When $f_m < f_s < f_r$: The input impedance of the resonant loop is inductive and the power switches S_1–S_4 achieve ZVS. When the converter works in the decoupling range, the resonant current on primary side is equal to the excitation inductance current and the transformer stops transferring energy to the secondary side. Therefore, the rectifier diode current naturally drops to zero to realize ZCS. At this status, the secondary side of the transformer loses its clamping effect on the excitation inductance. L_m (transformer inductance) combines with L_{r1} and C_{r1} to form a series resonance to achieve good soft-switching characteristics. So, under normal working conditions, try to keep the converter working in this frequency band.
2. When $f_s = f_r$: L_{r1}, C_{r1} become series resonant. The input impedance of the resonant loop is inductive. The DC voltage generates an AC square wave through the power switches and enters the transformer. The primary side switches realize ZVS and the secondary side diodes realize ZCS. The rectifier diode current is continuous, the converter has the highest efficiency, and the voltage gain is equal to 1 which is not affected by the load. This is the ideal operating point.

In order to analyze the gain characteristics of the converter under variable frequency control, the most commonly used First Harmonic Approximation (FHA) is adopted. In order to
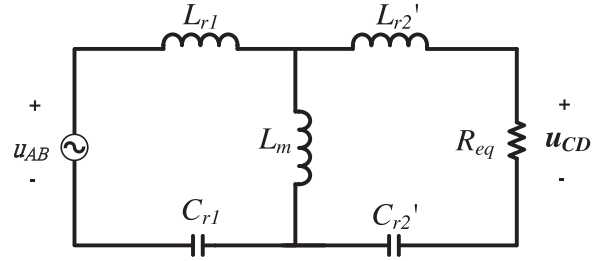

FIGURE 2 The equivalent circuit of the resonant tank

consider the battery charging voltage and power (the calculation of power needs resistance value, $P = V^2/R$, as shown in Equation (3) and (25), the battery is regarded as an equivalent resistance R_L. The AC equivalent load (R_{eq}) on secondary side of the transformer is shown in Equation (3) and the resonant devices L_{r2} and C_{r2} are mapped to the primary side. The equivalent circuit of the resonant tank is shown in Figure 2, where u_{AB} is input voltage, u_{CD} is output voltage, L_{r2}' and C_{r2}' are the inductance and capacitance, respectively, mapped from the secondary to the primary side of the transformer.

$$R_{eq} = n^2 \frac{8}{\pi^2} R_L \tag{3}$$

When analyzing the gain $M(j\omega)$ of the resonant tank, the gain can be obtained by using the input and output impedance of the resonant tank, as shown in Equation (4).

$$M(j\omega) = \frac{u_{CD}}{u_{AB}} = \frac{Z_m \parallel (Z_2 + R_{eq})}{Z_1 + Z_m \parallel (Z_2 + R_{eq})} \frac{R_{eq}}{Z_2 + R_{eq}} \tag{4}$$

The impedances of the primary and secondary resonant devices of the converter are shown in Equations (5)–(7), where ω_s is switching frequency.

$$Z_1 = j\omega_s L_{r1} + 1/(j\omega_s C_{r1}) \tag{5}$$

$$Z_2 = j\omega_s L_{r2} + 1/(j\omega_s C_{r2}) \tag{6}$$

$$Z_m = j\omega_s L_m \tag{7}$$

After calculation and simplification, the magnitude $G(\omega_n)$ of the gain of the resonant tank is obtained as Equation (8).

$$G(\omega_n) = |M(j\omega)|$$

$$= \frac{1}{\sqrt{\left(\frac{1}{k} - \frac{1}{k\omega_n^2} + 1\right)^2 + \left[\frac{Q}{k}\left(A\omega_n - \frac{B}{\omega_n} + \frac{C}{\omega_n^3}\right)\right]^2}}$$
(8)

where $A = k + kh + h$, $B = k + k/g + h + 1/g$, $C = 1/g$, normalized angular frequency $\omega_n = \omega_s/\omega_1$, quality factor $Q = \sqrt{L_{r1}/C_{r1}}/R_{eq}$, and resonant frequency ω_1.

In Equation (8), h is the resonant inductance ratio, g is the resonant capacitance ratio, and k is the ratio of magnetizing inductance to resonant inductance as shown in Equations (9)–(11), respectively.

$$h = L_{r2}'/L_{r1} = n^2 L_{r2}/L_{r1}$$
(9)

$$g = C_{r2}'/C_{r1} = C_{r2}/(n^2 C_{r1})$$
(10)

$$k = L_m/L_{r1}$$
(11)

Referring to Equation (8), the graph of converter gain magnitude versus normalized angular frequency for different quality factors Q is shown in Figure 3. The horizontal axis is the normalized angular frequency ω_n and the vertical axis is the converter voltage gain magnitude $G(\omega_n)$, where the quality factor Q also represents the load variation. When the Q value is larger, the load is heavier.

2.3 | Operation of phase-shift control

In order to achieve the voltage gain adjustment, the full-bridge phase shift control method was employed. The simultaneous turn-on time between the bridge legs was adjusted by changing the phase shift angle between the leading leg switches S_1, S_2 and the lagging leg switches S_3, S_4.
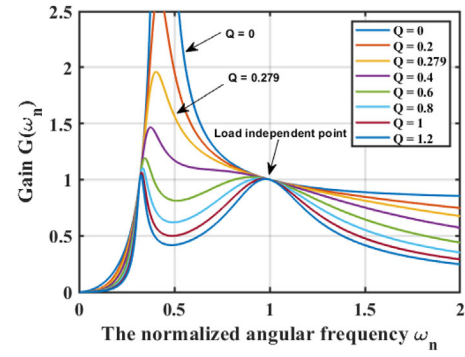

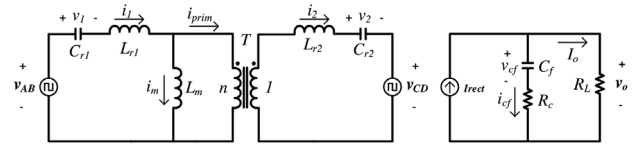**FIGURE 3** Gain magnitude curve of resonant tank with different Q values

FIGURE 4 Simplified diagram of CLLLC resonant converter

Describing Functions (EDF) method, which employed state-space average and harmonic approximation models [26]. The converter circuit is simplified to Figure 4. Let the resonant tank voltage and current be equivalent to sine and cosine components, respectively. By calculating with Kirchhoff's voltage law (KVL) and Kirchhoff's current law (KCL), the Equation (12) can be obtained, where V_{1s}, V_{2s}, I_{1s}, I_{2s}, V_{1c}, V_{2c}, I_{1c}, and I_{2c} are the sine and cosine components of the input voltage, input current, output voltage and out current, respectively.

The equivalent inductances are shown in Equations (13)–(15), the fundamental wave component of the input voltage of the resonant tank is shown in Equation (16), the harmonic

$$
\begin{bmatrix} V_e \\ V_e \\ 0 \\ 0 \\ 0 \\ 0 \\ 0 \\ 0 \end{bmatrix} =
\begin{bmatrix}
1 & \frac{L_{eq2}}{L_{eqm}} & 0 & \frac{L_{eq2}R_{eq}}{L_{eqm}} & 0 & 0 & -\omega_s L_{eq2} & 0 \\
1 & \frac{L_{eqm}}{L_{eq1}} & 0 & \frac{L_{eqm}R_{eq}}{L_{eq1}} & 0 & 0 & 0 & -\omega_s L_{eqm} \\
0 & 0 & 1 & 0 & \omega_s C_{r1} & 0 & 0 & 0 \\
0 & 0 & 0 & 1 & 0 & \omega_s C_{r2} & 0 & 0 \\
0 & 0 & \omega_s L_{eq2} & 0 & 1 & \frac{L_{eq2}}{L_{eqm}} & 0 & \frac{L_{eq2}R_{eq}}{L_{eqm}} \\
0 & 0 & 0 & \omega_s L_{eqm} & 1 & \frac{L_{eqm}}{L_{eq1}} & 0 & \frac{L_{eqm}R_{eq}}{L_{eq1}} \\
-\omega_s C_{r1} & 0 & 0 & 0 & 0 & 0 & 1 & 0 \\
0 & -\omega_s C_{r2} & 0 & 0 & 0 & 0 & 0 & 1
\end{bmatrix}
\times
\begin{bmatrix} V_{1s} \\ V_{2s} \\ I_{1s} \\ I_{2s} \\ V_{1c} \\ V_{2c} \\ I_{1c} \\ I_{2c} \end{bmatrix}
$$
(12)

In order to analyze the gain characteristics of the duty cycle in the resonant converter, Dalala et al. proposed the Extended

component of the output current of the resonant tank is composed of sine and cosine as shown in Equation (17) and the
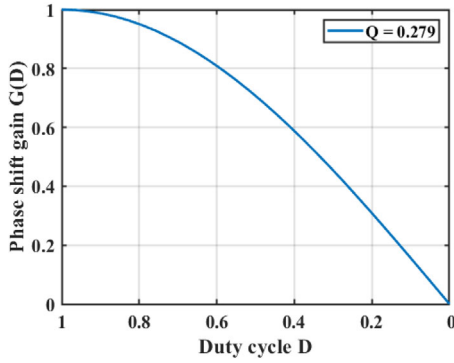
FIGURE 5 The converter's phase-shift gain versus duty cycle

output equivalent load is shown in Equation (18), where $L_{11} = L_1 + L_m$, $L_{22} = L_2' + L_m$, $L_2' = n^2 L_2$.

$$L_{eq1} = \frac{n^2 L_{11} L_{22} - L_m^2}{n^2 L_{11}} \tag{13}$$

$$L_{eq2} = \frac{n^2 L_{11} L_{22} - L_m^2}{n^2 L_{22}} \tag{14}$$

$$L_{eqm} = \frac{n^2 L_{11} L_{22} - L_m^2}{n L_m} \tag{15}$$

$$V_e = \frac{4}{\pi} \cdot V_1 \cdot \sin(\frac{\pi}{2} D) \quad 0 \leq D \leq 1 \tag{16}$$

$$I_{pk}^2 = I_{2s}^2 + I_{2c}^2 \tag{17}$$

$$R_{eq} = \frac{8}{\pi^2} R_L \tag{18}$$

$$V_o = \frac{2}{\pi} I_{pk} R_L \tag{19}$$

$$G(D) = \sin\left(\frac{D\pi}{2}\right) \tag{20}$$

It can be seen from Equations (12)–(19) that the voltage gain can be adjusted by changing the duty cycle D. In this study, the converter's phase-shift gain versus duty cycle is calculated from the above matrix and equations and the relation curve is shown in Figure 5 for $Q = 0.279$. The expression the $G(D)$ of the y-axis of Figure 5 is shown in Equation (20). As the duty cycle decreases, the gain becomes smaller. However, the converter phase shift duty cycle $D = 2T_{on}/T_s$, where T_{on} is the time when the switches (S_1, S_4 or S_2, S_3) turned on at the same time and T_s is the switching period. The variation range of T_{on} is 0–$T_s/2$, corresponding to the variation of duty cycle D equal to 0–1without considering the dead time.

3 | DESIGN OF THE RESONANT NETWORK

In order to enable the converter to achieve complete zero-voltage and zero-current soft switching in the forward and

reverse operating modes, the converter's operating frequency is designed in the range of $f_m < f_s \leqq f_r$. Therefore, when designing the resonant tank parameters, in addition to the converter gain, the soft switching characteristics are also taken into consideration. The following will design the parameters and analyze the converter gain characteristics.

3.1 | Transformer turns ratio *n*

In order to keep both advantages of phase shift and variable frequency control modes, this study uses the resonance frequency f_r as the demarcation point and divides it into two control modes. When the converter works at resonant frequency, the voltage gain is equal to 1 and the rated output voltage is 350 V. In the forward operation mode, the input voltage is 400 V and the output voltage is 250–450 V. Find the transformer turns ratio n in Equation (20). V_{2nom} is the nominal voltage.

$$n = \frac{V_1}{V_{2nom}} = \frac{400}{350} \simeq 1.14 \tag{21}$$

Then, the maximum and minimum gains required for the resonant tank need to be calculated first for subsequent resonant parameter design.

$$G_{max} = \frac{nV_{2max}}{V_1} = \frac{1.14 \times 450}{400} \simeq 1.28 \tag{22}$$

$$G_{min} = \frac{nV_{2min}}{V_1} = \frac{1.14 \times 250}{400} \simeq 0.71 \tag{23}$$

The converter adopts frequency conversion control in boost mode and phase shift control in buck mode. Therefore, the maximum gain requirement should be considered at the same time in the analysis of soft switching conditions.

3.2 | Magnetizing inductance L_m

When the switch operation frequency is the resonant frequency (i.e. the resonant period is equal to the switching period) and the converter works in the dead time, the magnetizing inductance current reaches the maximum value. This is the charging and discharging stage of parasitic capacitance of switches. The magnetizing inductance current is large enough to ensure that the parasitic capacitance completes the energy exchange to let the capacitance finish charging and discharging and the switches achieve zero-voltage soft switching (ZVS). By using the current formulae of magnetizing inductance and parasitic capacitance, the Equation (23) is calculated, where the switching period T_s is the resonant period 1/(100 KHz), C_{oss} is the parasitic capacitance of switches. Considering the turn-on time t_{on} and turn-off time t_{off} of the power switches, the dead time T_d 200 ns is used.

$$L_m \leq \frac{T_s T_d}{16 C_{oss}} = \frac{\frac{1}{100 \times 10^3} \times 200 \times 10^{-9}}{16 \times 55 \times 10^{-12}} = 2.27 mH \tag{24}$$
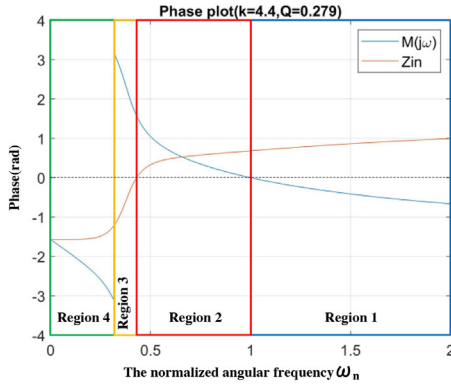
FIGURE 6 Phase diagram of converter gain and input impedance

3.3 | Quality factor Q and inductance coefficient k

In order to ensure that the converter can achieve complete zero-voltage and zero-current soft switching in the range of $f_m < f_s \leqq f_r$, the input impedance and gain characteristics of the resonant tank were employed and analyzed when selecting the quality factor Q and the inductance coefficient k. The gain is shown in Equation (4) and the input impedance of resonant tank is shown in Equation (24). The circuit is shown in Figure 2.

$$Z_{in} = Z_1 + Z_m \parallel (Z_2 + R_{eq}) \tag{25}$$

The AC equivalent load is shown in Equation (25). The parameter design is based on the maximum power of the converter to ensure that the converter can achieve soft

$$R_{eq} = n^2 \frac{8}{\pi^2} \frac{V_{2nom}^2}{P_o} = (1.14)^2 \frac{8}{\pi^2} \frac{350^2}{1000} \simeq 129\Omega \neq \tag{26}$$

switching in the full range and full load.

In the soft switching interval, the converter considering the maximum gain requirement and the gain tunable ability with the variable frequency, it is necessary to strike a balance between the two. Referring to the gain characteristics of Figure 3 and the Equation (21), parameters $Q = 0.279$ and $k = 4.4$ were selected for analysis. The phase diagram of input impedance Z_{in} and gain $M(jw)$ is shown in Figure 6. When the converter operation frequency is in region 2, the input impedance is inductive and the magnetizing inductance joins the resonance, which can realize ZVS and ZCS soft switching.

3.4 | Resonant parameters

From the gain magnitude calculation of Equation (8), the converter efficiency of the output power P of the resonant tank to the rated output power P_o can be obtained in Equation (26). The converter efficiency is related to the resonant capacitance ratio h and resonant inductance ratio g as shown in Equations (9) and (10), respectively. When the converter works at the resonant fre-
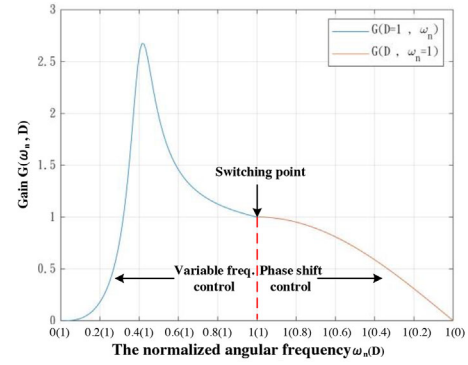

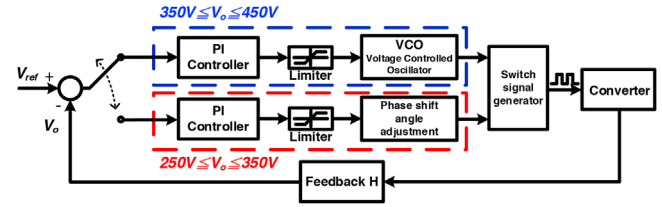**FIGURE 7** Gain curve of hybrid switching control

FIGURE 8 Theoretical diagram of hybrid switching control

quency, that is. $\omega_n = 1$, the converter efficiency could be the best when $gh = 1$ in theory. Therefore, in order to have the advantages of LLC resonant circuit, the ratio of resonant capacitor to resonant inductance was set to 1 in this study.

$$\eta = \frac{P}{P_o} = \frac{u_{AB}^2}{R_{eq}P_o} \frac{1}{1 + Q^2 \times \left(h - \frac{1}{g}\right)^2} \tag{27}$$

4 | HYBRID CONTROL STRATEGY

4.1 | Hybrid-switching control

The hybrid switching control mainly adopts two modes of fixed-phase-shift and variable frequency control or fixed-frequency and phase-shift control, as shown in Figure 7. In the buck mode, the operation frequency is fixed and the phase-shift angle is adjusted (that is, the duty cycle D is adjusted, $D = 1$, i.e. 100%) to achieve the voltage regulation. In the boost mode, the phase-shift angle is fixed and the operation frequency is adjusted, using the characteristics of the resonance circuit to achieve the buck-boost regulation. Meanwhile, the switching point must set up between the variable frequency control and the phase-shift control. Considering the converter efficiency, the switching point is set at the resonant frequency f_r.

As shown in Figure 8, when the hybrid switching control adopts two proportional integral (PI) controllers for compensation, it is an ideal model and only suitable for open loop control. As the load changes (250–350 V or 350–450 V), the gain characteristics also change, causing the converter to be
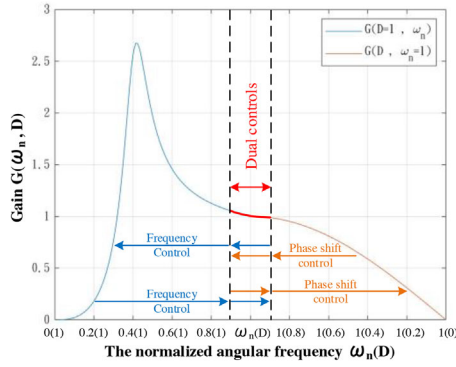
FIGURE 9 Gain curve of hybrid switching with dual controls

unable to accurately define the switching point, causing inrush during mode switching or failing to switch smoothly [29].

4.2 | Hybrid switching with dual controls

In order to have the advantages of both variable frequency and phase-shift hybrid switching control, this paper proposes a hybrid dual-control method, as shown in Figure 9. Based on the ideal hybrid-switching control, a "dual-control interval" is provided to achieve close loop control, which combines variable frequency and phase-shift control, as shown in Figure 10a.

When the converter transfers from boost mode to buck mode ($\rightarrow$), the variable frequency (@ phase-shift angle fixed) control mode is adopted first as the frequency gradually increases. When the dual-control interval is reached, the dual controls (both variable frequency and phase-shift control) are employed to adjust the converter. Then, the converter continues in buck mode (voltage decreased) and the switching frequency is increased to the maximum operating frequency. The control mode is then changed to the phase-shift (@ frequency fixed) control mode for the converter.

Conversely, if the converter transfers from buck mode to boost mode ($\leftarrow$), the phase shift (@ frequency fixed) control mode is first adopted with the phase shift angle decreasing (i.e. the duty cycle D increasing). When the dual-control interval is reached, the dual controls (both variable frequency and phase-shift control) are employed to adjust the converter. Then, the converter continues in boost mode (voltage increased) and the duty cycle is increased to the maximum value. The control mode is then changed to the variable frequency (@ phase shift angle fixed) control mode for the converter.

When designing the controller, output voltage was used as the condition for switching judgment, as shown in Figure 10. In this study, in the forward charging mode, the input voltage was 400 V, while the output voltage spanned a wide range of 250–450 V. So, 350 V is selected as the switching center point and ±10 V range is selected as the hybrid dual-control interval. If the output voltage of the converter was lower than 340 V ($V_{sw\ min}$), the phase shift (@ constant frequency) control was used.

When the converter output voltage exceeded 340 V but was <360 V ($V_{sw\ max}$), the converter would switch to the hybrid dual-
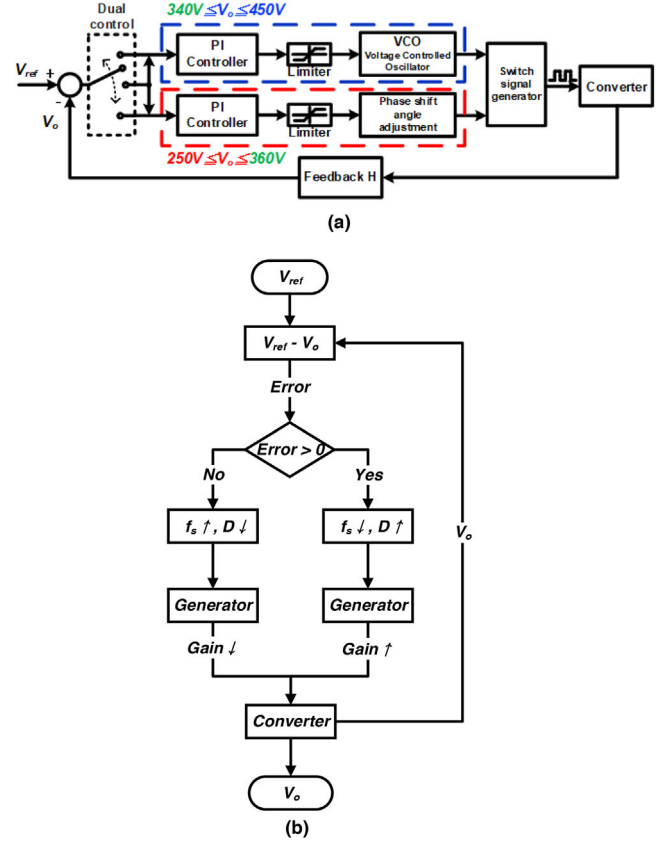

FIGURE 10 (a) Theoretical diagram of hybrid switching with dual controls. (b) The control flow chart for hybrid switching with dual controls

control mode where both phase shift and variable frequency control were employed. If the output voltage of the converter exceeded 360 V, the converter would switch to the variable frequency (@ constant phase shift angle) control mode. The gain characteristics of the control mode of the converter must be considered when selecting the dual-control interval. Since various converters have different loads, the switching interval needs to match the load of the converter. The smaller the dual control interval, the more advantageous the converter's efficiency.

The strategy in this paper was proposed to improve the processes for switching between variable frequency and phase shift control, overcome the shortcomings of hybrid switching control, and solve the problem of switching surge or failure of smooth switching caused by the design difficulty of the switching point of the converter under different loads. When the converter works at the switching point, the hybrid dual control interval is used as a buffer controller, which may reduce the switching surge, as well as smoothly switch to obtain the constant voltage and constant current output. This kind of converter has many advantages of applications in wide load and wide voltage range.

The digital signal processor (DSP) (Texas Instrument TMS320F28335) and programming are used to adjust the mode switch and achieve this dual-control. In dual-control mode, variable frequency control and phase shift control each participate in the gain adjustment at the same time. When the converter

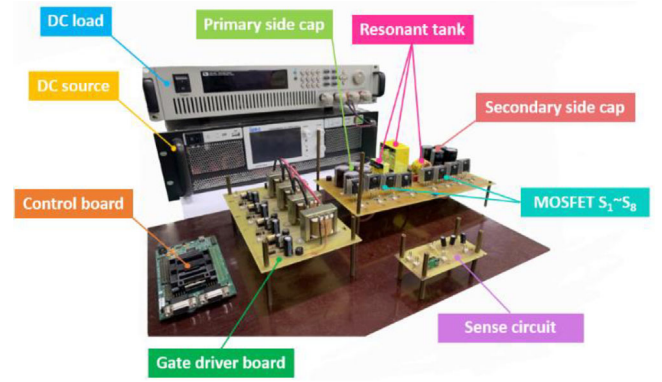**TABLE 1** Device parameters of reversible hybrid control resonant converter

Devices	Type/values
$S_1 - S_8$	C2M0160120D
n	1.14
L_{r1}	57.59 μH
L_{r2}	48.5 μH
L_m (measured)	253 μH
C_{r1}	44 nF
C_{r2}	55 nF
C_1, C_2	600 μF

FIGURE 11 Experimental setup of the platform on which hardware implementation is performed

requires a larger gain, that is, $Error > 0$ ($Error = V_{ref} - V_o$), both the switching frequency and the phase shift angle are reduced (duty cycle increases) to achieve boost characteristics, as shown in Figure 10b. When the converter requires a smaller gain, that is, $Error \leq 0$, both the switching frequency and the phase shift angle increase (the duty cycle decreases) to achieve the buck characteristics, as shown in Figure 10b. The converter switching frequency f_s is $f_m < f_s \leq f_r$, and the duty cycle D is $0 < D \leq 1$.

5 | EXPERIMENTAL VERIFICATIONS

Here, we studied the second-stage DC–DC converter of the bidirectional vehicle energy storage system. The load of the converter is an electric vehicle battery pack composed of general lithium batteries in series and parallel. The charging voltage of most electric vehicle battery packs is in the range of 250–450 V. The working modes of the converter in this study are divided into forward charging and reverse discharging modes. Therefore, the input voltage of the converter needs to be fixed during forward charging mode to achieve a wide range of output voltages. Meanwhile, during reverse discharging mode, the converter should accept a wide range of input voltage and maintain output voltage constant (fixed). The device parameters in the converter are shown in Table 1. The experimental setup picture is as shown in Figure 11. The Texas Instruments MCU F28335 control board was employed to programming, to output PWM signal to the Gate driver board to drive the power MOSFET, and to sample the output voltage and current signals from the Sense circuit to achieve the closed-loop variable frequency control and phase shift control. In the forward charging mode, the constant voltage (CV) mode of the DC source is used to simulate the primary side V_1 power supply, and the constant current (CC)/CV mode of the DC load is employed to simulate the charging of the battery V_2. Conversely, in the reverse discharge mode, the CV mode of the DC source is used to simulate the discharge of the secondary side battery V_2, and the CC mode of the DC load is employed to simulate the primary side output voltage V_1.

For maximum gain $G_{max} = 1.28$ as shown in Equre (21), and $Q = 0.279$, $k = 4.4$ selected, then C_{r1} and L_{r1} can be calculated

as follows:

$$C_{r1} = \frac{1}{2\pi f_{r1} R_{eq} Q} = \frac{1}{2 \times \pi \times (100 \times 10^3) \times 129 \times 0.279}$$
$$\simeq 43.9 \text{ nF} \quad (28)$$

From above Equation (27), C_{r1} 43.9 nF is obtained, so 44 nF resonant capacitor was chosen.

$$L_{r1} = \frac{Q R_{eq}}{2\pi f_{r1}} = \frac{0.279 \times 129}{2 \times \pi \times 100 \times 10^3} \simeq 57.59 ^-H \quad (29)$$

$$L_m = k L_{r1} = 4.4 \times 57.59 ^-H \simeq 253 ^-H \quad (30)$$

$$C_{r2} = g n^2 C_{r1} = 1 \times 1.14^2 \times 43.9 \times 10^{-9} \simeq {}^-H \quad (31)$$

From above Equation (30), C_{r2} 57.45 nF is obtained, so 55 nF resonant capacitor was chosen.

$$L_{r2} = \frac{h L_{r1}}{n^2} = \frac{1 \times 57.59 \times 10^6}{1.14^2} \simeq 48.5 ^-H \quad (32)$$

5.1 | Converter operation in the FBCM

In forward battery charging mode (FBCM), the experiment was conducted with an input voltage of 400 V and output current fixed at 2.2 A. The output voltage covers a range from 250 to 450 V, and the maximum power can reach 1000 W. The output of the converter simulates the charging voltage range of the battery pack in the electric vehicle. The converter characteristics were measured at the minimum conversion voltage of 250 V and the maximum conversion voltage of 450 V.

In forward charging mode, Figure 12 shows the measured experimental waveforms of the primary side resonant current i_{Lr1}, the secondary side resonant current i_{Lr2} and the primary side resonant tank voltage v_{AB}. Figure 12a shows the waveforms measured at output voltage 250 V. When the output voltage was 250 V, the power switch (MOSFET $S_1 - S_4$) of the converter worked at the resonant frequency, and the gain was controlled
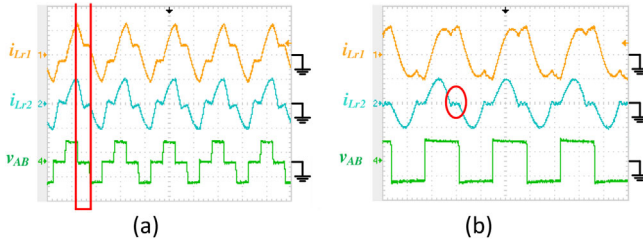
FIGURE 12 Experimental waveforms of resonance voltage and current in FBCM: (a) Measured at output voltage 250 V, (b) measured at output voltage 450 V
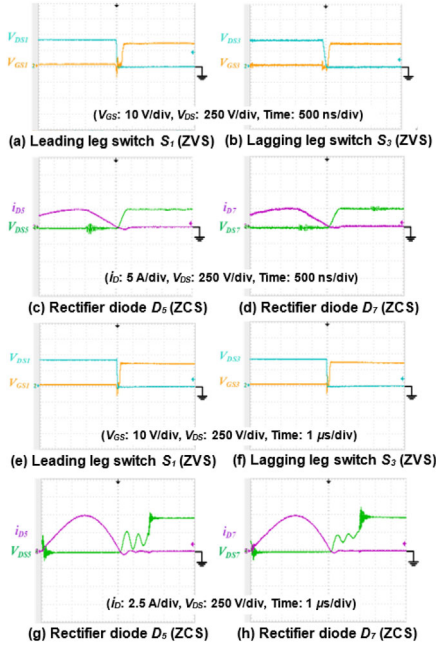

FIGURE 13 The experimental waveforms of switches realizing ZVS and ZCS in forward charging mode: (a–d) output voltage 250 V, (e–h) output voltage 450 V

FIGURE 14 Experimental waveforms of I_2: (a, b) in the phase shift control mode, where V_2 is switched back and forth from 250 to 300 V. (c, d) in the variable frequency control mode, where V_2 is switched back and forth from 400 to 430 V

by phase shift control (@ constant frequency). When the resonant tank voltage in the primary side was 0 (changing from high to zero), the resonant current in the primary side i_{Lr1} dropped as marked red in Figure 12a, and the converter entered the decoupling interval (where the transformer cannot transfer energy). Figure 12b shows the waveforms measured at output voltage 450 V. When the output voltage was 450 V, the power switch of the converter worked in the frequency range $f_m < f_s \leqq f_r$, the gain was adjusted by variable frequency control (@ constant phase shift angle). The resonant tank voltage is an AC square wave. When the converter works in the decoupling interval, the transformer cannot transfer energy, and the resonant current in the secondary side i_{Lr2} is discontinuous (as marked by red circle in Figure 12b).

Figure 13 shows the experimental waveforms measured in forward charging mode, where (a)–(d) are from output voltage 250 V, (e)–(h) are from output voltage 450 V, and the output current is kept constant at 2.22 A. In the primary side, the measurement waveforms of voltage V_{DS} of leading leg switch S_1
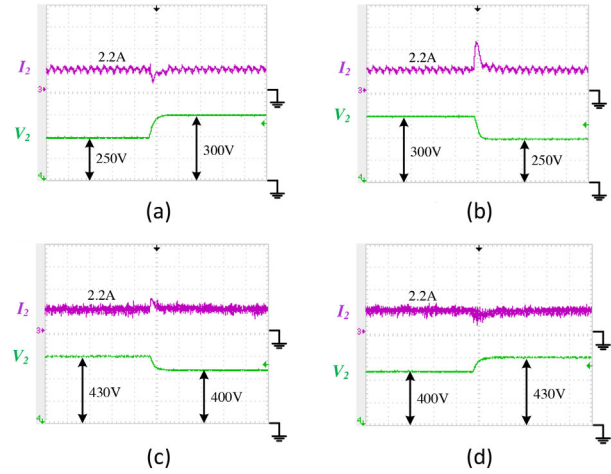
and lagging leg switch S_3 are shown in Figures 13a and 13e and then 13b and 13f, respectively, which shows that zero-voltage soft switching (ZVS) is realized. In the secondary side, the measurement waveforms of the currents of diodes D_5 and D_7 of switches S_5 and S_7, respectively, in the rectifier circuit are shown in Figure 13c,d,g,h, which demonstrates that zero-current switching (ZCS) is realized. Figure 13 also shows the waveforms of drive signal V_{GS} of the power switch, switch voltage V_{DS}, and switch diode current i_D. When the switch diode was turned off, the oscillation waveform of V_{DS} voltage was consistent with the simulation result, being caused by the resonance of the parasitic capacitance in the rectifier switch. When the converter was in forward charging mode, the input voltage was set to 400 V, and the output voltage V_2 was modulated with a dynamic load to simulate the charging voltage of the electric vehicle battery pack. The converter working in the constant current (CC) mode is then tested to check whether the closed-loop control of the output current I_2 worked normally or not. Figure 14a,b shows the results in the phase shift control mode, where the output voltage V_2 was switched back and forth from 250 to 300 V. Figure 14c,d indicates the results in the variable frequency control mode, where the output voltage V_2 was switched back and forth from 400 to 430 V. All the I_2 current waveforms in Figure 14 show that at the moment of voltage switching, the output current I_2 can be compensated to a constant current of 2.2 A by the controller (as shown in Figure 10).

When the converter was in forward charging mode, the input voltage was set to 400 V, and the output voltage I_2 was modulated with a dynamic load to simulate the charging current of the electric vehicle battery pack. Then, the converter working in the constant voltage (CV) mode was tested to check whether the closed-loop control of the output voltage V_2 was stable or not. Figure 15 demonstrates using dynamic load to simulate the battery charging current switching back and forth from 1 to 2 A, where in (a) (b) the output voltage was set at 260 V under phase
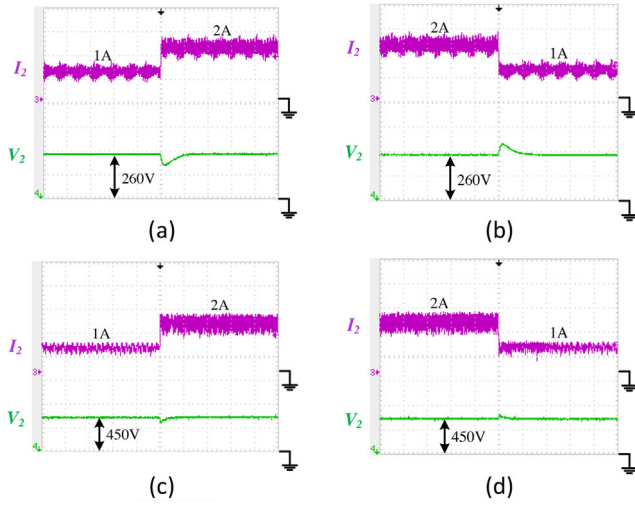
FIGURE 15   In forward charging mode, the experimental waveforms of V_2 when charging current switching back and forth from 1 to 2 A: (a, b) V_2 s set at 260 V under phase shift control mode, and (c, d) V_2 is set at 450 V under variable frequency control mode
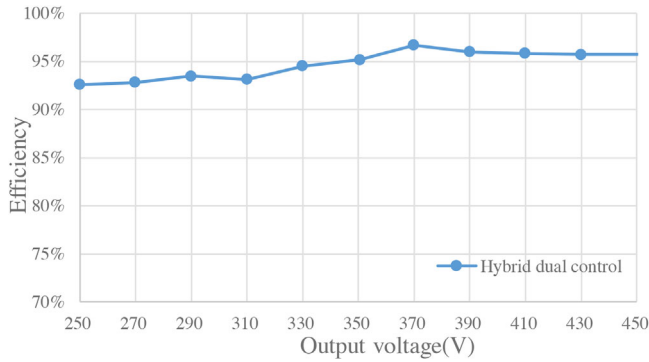

FIGURE 16   Relationship of converter efficiency versus output voltage in FBCM with hybrid switching with dual controls

shift control mode, and in (c)(d) the output voltage was set at 450 V under variable frequency control mode. The V_2 voltage waveform in Figure 15 indicates that at the moment of current switching, the output voltage can be compensated to a constant voltage value by the controller.

When the converter works in forward charging mode and the output current is kept constant, the relationship of converter efficiency versus output voltage in a wide range of 250–450 V is shown in Figure 16. When the converter's operating frequency approaches the resonance frequency, the transformer decoupling interval becomes smaller, thus reducing the loss on the magnetizing inductance. At this point, the efficiency is highest, as shown in Figure 16. When the output voltage is 370 V, the highest conversion efficiency reaches 96.69%. Furthermore, when the converter output voltage for the battery charging is decreased, the phase shift angle and the peak value of the resonant current increase, which subsequently increases the conduction loss and reduces converter efficiency. As shown in Figure 16, when the output voltage is 250 V, the converter efficiency is 92.56%.
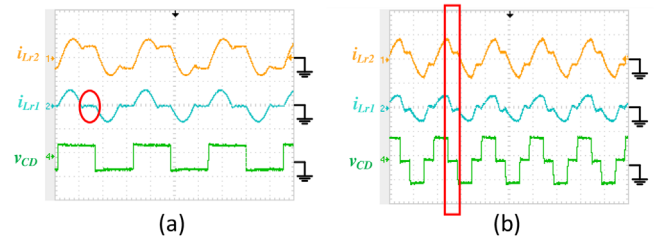

FIGURE 17   Experimental waveforms of resonance voltage and current in RBDM in reverse discharging mode: (a) Measured at input voltage 250 V, (b) measured at input voltage 450 V

5.2 | Converter operation in the RBDM

This section discusses the situation where the converter works in reverse battery discharge mode (RBDM). The battery pack voltage of an electric vehicle is used as the input voltage, with the busbar as the output voltage. The input voltage range was 250–450 V and the output voltage was 400 V. The experiment was carried out in constant output voltage mode, and the maximum power was 1000 W. In the reverse discharging mode, Figure 16 shows the measured experimental waveforms of the primary side resonant current i_{Lr1}, the secondary side resonant current i_{Lr2}, and the secondary side resonant tank voltage v_{CD}.

Figure 17a shows the waveforms measured at input voltage 250 V. When the input voltage was 250 V, the power switch of the converter worked in the frequency range $f_m < f_s \leqq f_r$, and the gain was adjusted by variable frequency control (@ constant phase shift angle). The resonant tank voltage was an AC square wave. When the converter worked in the decoupling interval, the transformer could not transfer energy and the resonant current in primary side i_{Lr1} was discontinuous (as marked by red circle in Figure 17a).

Figure 17b shows the waveforms measured at input voltage 450 V. When the input voltage was 450 V, the power switch (MOSFET S_1–S_4) of the converter worked at the resonant frequency, and the gain was controlled by phase shift control (@ constant frequency). When the resonant tank voltage in the secondary side was 0 (changing from high to zero), the resonant current in the secondary side i_{Lr2} dropped, as marked red in Figure 17b, and the converter entered the decoupling interval (where the transformer could not transfer energy to the primary side), so the primary side resonant current i_{Lr1} was discontinuous.

Figure 18 shows the experimental waveforms measured in reverse discharging mode, where (a)–(d) were from input voltage 250 V, (e)–(h) were from input voltage 450 V, the output voltage was 400 V and output current was kept constant at 2.5 A. In the secondary side, the measurement waveforms of the voltage V_{DS} of the lagging leg switch S_5 and the leading leg switch S_7 are shown in Figure 18a and 18e and then 18b and 18f, respectively, indicating that zero-voltage soft switching (ZVS) is realized. In the primary side, the measurement waveforms of the currents of diodes D_1 and D_3 of switches S_1 and S_3, respectively, in the rectifier circuit are shown in Figure 18c,d,g,h, which

(VGS: 10 V/div, VDS: 250 V/div, Time: 1 μs/div)

(a) Lagging leg switch S_5 (ZVS) (b) Leading leg switch S_7 (ZVS)

(iD: 5 A/div, VDS: 500 V/div, Time: 1 μs/div)

(c) Rectifier diode D_1 (ZCS) (d) Rectifier diode D_3 (ZCS)

(VGS: 10 V/div, VDS: 250 V/div, Time: 500 ns/div)

(e) Lagging leg switch S_5 (ZVS) (f) Leading leg switch S_7 (ZVS)

(iD: 5 A/div, VDS: 500 V/div, Time: 500 ns/div)

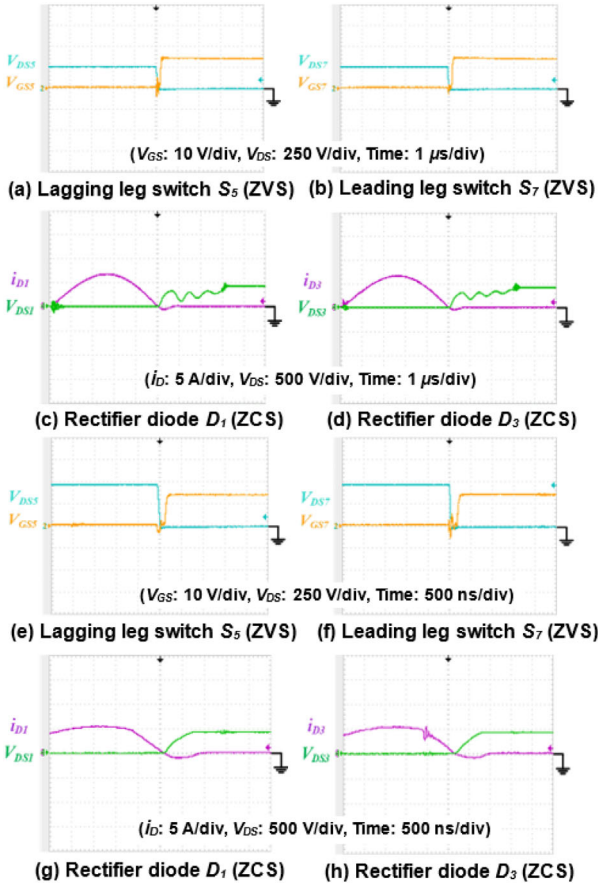(g) Rectifier diode D_1 (ZCS) (h) Rectifier diode D_3 (ZCS)

FIGURE 18 In reverse discharge mode, the experimental waveforms of switches realizing ZVS and ZCS: (a–d) Input voltage 250 V, output voltage 400 V and constant current 2.5 A. (e–h) Input voltage 450 V, output voltage 400 V and constant current 2.5 A

FIGURE 19 In reverse discharging mode, the experimental waveforms of V_1 when discharging: (a, b) V_2 is set at 260 V and the bus current is modulated back and forth from 1.25 to 2.5 A under phase shift control mode, and (c, d) V_2 is modulated between 250 and 260 V under variable frequency control mode

FIGURE 20 Converter efficiency versus input voltage with hybrid switching with dual controls mode in RBDM

demonstrates that zero-current soft switching (ZCS) is realized. Figure 18 also shows the waveforms of drive signal V_{GS} of the power switch, switch voltage V_{DS}, and switch diode current i_D. When the switch diode is turned off, the oscillation waveform of V_{DS} voltage is consistent with the simulation result, being caused by the resonance of the parasitic capacitance in the rectifier switch.

In reverse discharging mode, the battery pack of an electric vehicle is employed as converter input voltage V_2 to transfer energy to the bus (i.e. voltage V_1). The input voltage range was 250–450 V, and the output voltage V_1 was set to 400 V. In order to supply a stable bus voltage, the converter adopted the constant voltage (CV) working mode. Then the converter working in the CV mode was tested to check whether the closed-loop control of the output voltage V_1 worked normally or not. As shown in Figure 19a,b, the bus current was modulated with a dynamic load to simulate the discharging current, switching back and forth from 1.25 to 2.5 A. As shown in Figure 19c,d, the DC power supply was used to simulate the electric vehicle battery pack to provide input voltage V_2 switching back and forth between 250–260 V (wide range characteristics); then the converter worked in constant voltage mode, and the stability of output voltage V_1 was tested. All the V_1 voltage waveforms in
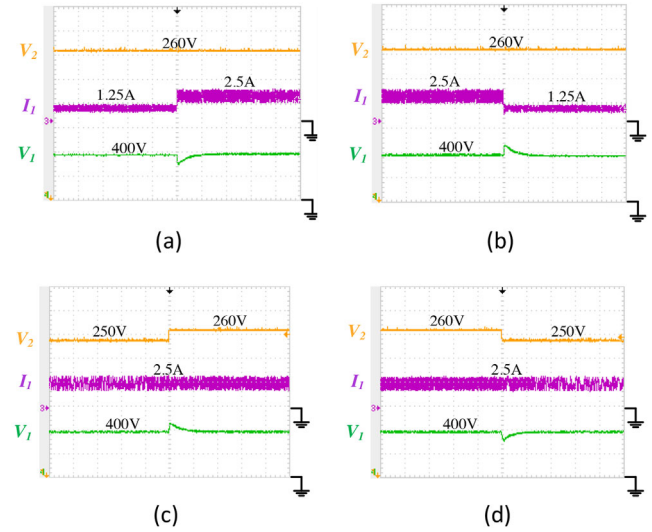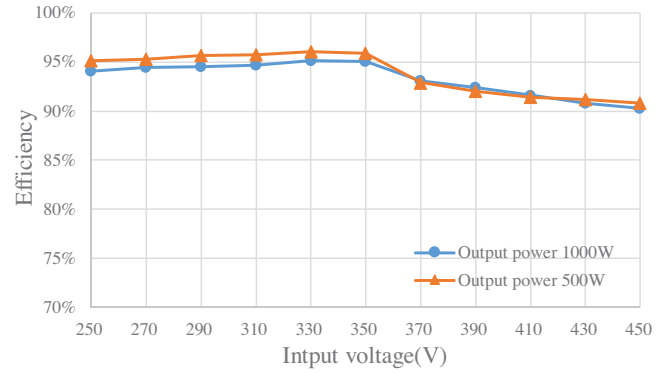
Figure 19 show that at instances of current or voltage switching, the output voltage V_1 can be compensated to a constant voltage value by the controller.

Figure 20 shows the efficiency curves of the converter with output power of 1000 and 500 W in reverse discharge mode. The input spans a wide range voltage of 250–450 V, and the output was a constant voltage of 400 V. The dynamic load simulated the load of the output bus. When the converter worked in CV mode and the operating frequency was close to the resonance frequency, the transformer decoupling interval grew smaller, thus reducing the loss on the magnetizing inductance. When the input voltage was 330 V, the highest conversion efficiency could reach 96.02% (power 500 W). Furthermore, DC power supply was employed to simulate the battery pack of the electric vehicle to provide the input voltage. When the input battery voltage was 450 V, the converter worked in phase shift control mode, with the largest phase shift angle and the smallest
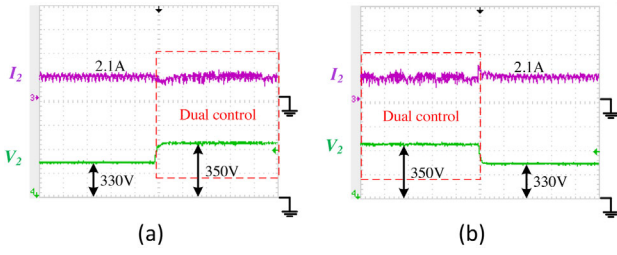
FIGURE 21 The waveforms of converter output voltage V_2 and output current I_2, switched between phase shift control (@constant frequency) and hybrid switching with dual controls

FIGURE 22 Comparisons of efficiency curves of converter by variable frequency control with that by hybrid dual control in FBCM

TABLE 2 Comparisons of MOSFET parameters

S_1–S_8 parameters	C2M0160120D	UJ3C065080K3S
V_{FSD}	3.3 V	1.5 V
$R_{ds(on)}$	160 mΩ	80 mΩ
V_{DS}	1200 V	650 V
I_{DS}	19 A	31 A
C_{OSS}	47 pF	104 pF
t_{rr}	23 ns	16 ns

duty cycle, so the current peak value was large. The conduction loss increased, while the converter efficiency decreased. In Figure 20, when the input voltage was 450 V, and the output power was 1000 W, the converter efficiency was 90.29%. The MOSFETs C2M0160120D were used in the experiment.

5.3 | Hybrid switching with dual controls

In this section, the experimental test of forward battery charging mode is carried out to examine the performance of constant current output I_2 of the converter with the hybrid dual control mode (as shown in the gain curve of Figure 9). The input voltage was 400 V, and the output terminal was simulated as a battery by the dynamic load. The output voltage V_2 was modulated between 330 and 350 V. Figure 21 shows the waveforms of converter output voltage V_2 and output current I_2: When (a) the converter switches from phase shift control (@ constant frequency) to dual controls; (b) from dual controls to phase shift control (@ constant frequency). The results of the two experiments indicate that this control strategy is successful, and I_2 can be controlled at a constant current of 2.1 A.

5.4 | Efficiency comparison

In this section, we discuss the converter in the forward charging mode, the constant current mode, and buck mode (that is, the output voltage is lower in the range of 250–350 V). The conversion efficiency converted with phase shift control is compared with variable frequency control. Dynamic load was employed to simulate the charging voltage of the electric vehicle battery. When the converter's operating frequency was higher than the resonant frequency, the transformer has no decoupling interval, the rectifier diode in the converter could not achieve zero-current soft (ZCS) switching, and the switching frequency continued to increase. These factors led to an increase in switching losses via variable frequency control mode. Figure 22 demonstrates that the control strategy, hybrid dual control, proposed in this study for the converter has higher efficiency than traditional full variable-frequency control in buck mode ($V_2 < 350$ V). The MOSFETs C2M0160120D were used in the experiment.
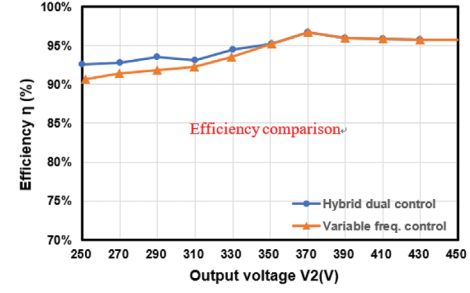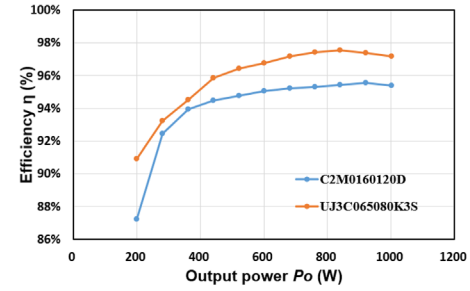

FIGURE 23 The efficiency curves with respect to power levels of CLLLC resonant converter in FBCM mode using C2M0160120D and UJ3C065080K3S power switches, respectively

When measuring the efficiency of the CLLLC resonant converter with regard to the power levels, the UJ3C065080K3S power switch was employed instead of the silicon carbide power MOSFET C2M0160120D [31]. UJ3C065080K3S is based on a unique cascode circuit configuration [32]. The parameter comparisons of the two power switches are shown in Table 2, where V_{FSD} is the body diode forward voltage.

The V_{FSD} of C2M0160120D and UJ3C065080K3S are 3.3 and 1.5 V, respectively. The V_{FSD} of C2M0160120D is greater than that of UJ3C065080K3S, which results in heat generation and energy loss during secondary side rectification in the CLLLC converter (during MOSFET on to off switching). After changing to use UJ3C065080K3S, the temperature of the power switch decreases, the energy loss is reduced, and the converter conversion efficiency is improved. Figure 23 shows the conversion efficiency versus the output power from 200 to 1000 W. The maximum efficiency was 97.57 % when the output power was 840 W, as shown in Figure 23.

6 | CONCLUSION

In this research, we have proposed a reversible hybrid switching dual-control resonant converter that can be applied to an electric vehicle battery charging and discharging system. Its circuit architecture is mainly composed of a symmetrical LLC resonant converter. The switching strategy of reversible hybrid control with both phase shift and variable frequency controls was developed to improve the traditional resonant converter. The converter achieved bidirectional buck/boost conversion in a wide voltage range with soft switching having zero voltage and zero current switching. This system can also resolve the problems of only using variable frequency control, that the voltage is not easy to adjust at light loads, and switching loss increases at high frequencies.

In the forward charging mode, the input voltage was 400 V, the output voltage was 250–450 V, the maximum power was 1000 W, and the maximum conversion efficiency was 96.69%. In reverse discharge mode, the input voltage was 250–450 V, the output voltage was 400 V, the maximum power was 1000 W, and the conversion efficiency at full load was 95.13% @ 330 V. The maximum conversion efficiency was 97.57% when the output power was 840 W when using UJ3C065080K3S as power switches.

The characteristics of the converter developed in this study are as follows:

1. Both forward and reverse directions can be converted in a wide voltage range with soft switching having zero voltage and zero current switching: Although the traditional bidirectional DC–DC converter architecture has bidirectional conversion characteristics, achieving high conversion efficiency in both directions is difficult. This research adopts the hybrid switching with dual control strategy, combining the advantages of variable frequency and phase shift control to improve both forward and reverse converter efficiency and achieve bidirectional soft switching in a wide voltage range having zero voltage and zero current switching.
2. Improving the problems of only using variable frequency control, that the voltage is not easy to adjust at light loads, and switching loss increases at high frequencies: The traditional resonant converter adopts variable frequency control. Although it has both buck and boost modes, the voltage in buck mode is not easy to adjust at light loads, and the variable frequency range is too wide, which makes it difficult to optimize magnetic devices. Therefore, in this study, we proposed a hybrid control strategy. In addition to the variable frequency control used in the traditional resonant circuit, phase shift control is also employed in this study. By modulating the phase angle difference between the leading and the lagging leg switches, the buck function is achieved, the switching loss is reduced, and the problem that the voltage is not easy to adjust at light loads is resolved.
3. Proposing hybrid switching with a dual-control strategy to overcome the design difficulty of hybrid switching control with a digital method: The hybrid switching with dual controls is mainly divided into hybrid switching control and

dual controls. If the hybrid switching control is adopted, its switching point is not easily determined in the design; if dual controls are adopted, the phase shift control is also adopted under variable frequency control, which is likely to cause the system instability and increase conduction loss. Therefore, this study combines the advantages of the two control modes with the goal of narrowing the dual control interval, and proposes a hybrid switching with dual control strategy to enhance control superiority.
4. Proposing a closed loop control of a resonant converter with hybrid switching with dual controls: Since the switching point of the hybrid switching control cannot be precisely determined in an easy way, realizing the closed loop control of the converter is difficult.

In addition to proposing a hybrid switching with dual control strategy, circuit experiments are also used to verify the feasibility of the control strategy, which can improve the shortcomings of hybrid switching control.

ORCID
Jeng-Yue Chen https://orcid.org/0000-0001-8214-4208

REFERENCES

1. Xuan, Y., Yang, X., Chen, W., Liu, T., Hao, X.: A novel three-level CLLC resonant DC–DC converter for bidirectional EV charger in DC microgrids. IEEE Trans. Ind. Electron. 68(3), 2334–2344 (2021)
2. Emamalipour, R., Lam, J.: A hybrid string-inverter/rectifier soft-switched bidirectional DC/DC converter. IEEE Trans. Power Electron. 35(8), 8200–8214 (2020)
3. Li, B., Li, Q., Lee, F.C., Liu, Z., Yang, Y.: A high efficiency high-density wide-bandgap device-based bidirectional onboard charger. IEEE J. Emerging Sel. Topics Power Electron. 6(3), 1627–1636 (2018)
4. Zhang, C., Li, P., Kan, Z., Chai, X., Guo, X.: Integrated half-bridge CLLC bidirectional converter for energy storage systems. IEEE Trans. Ind. Electron. 65(5), 3879–3889 (2018)
5. Liu, Y., Chen, C., Chen, K., Syu, Y., Dung, N.: High-frequency and high-efficiency isolated two-stage bidirectional DC–DC converter for residential energy storage systems. IEEE J. Emerging Sel. Top. Power Electron. 8(3), 1994–2006 (2020)
6. Huang, J., Xiao, J., Wen, C., Wang, P., Zhang, A.: Implementation of bidirectional resonant DC transformer in hybrid AC/DC micro-grid. IEEE Trans. Smart Grid 10(2), 1532–1542 (2019)
7. Bal, S., Yelaverthi, D.B., Rathore, A.K., Srinivasan, D.: Improved modulation strategy using dual phase shift modulation for active commutated current-fed dual active bridge," IEEE Trans. Power Electron. 33(9), 7359–7375 (2018)
8. Yan, Y., Bai, H., Foote, A., Wang, W.: Securing full-power-range zero-voltage switching in both steady-state and transient operations for a dual-active-bridge-based bidirectional electric vehicle charger. IEEE Trans. Power Electron. 35(7), 7506–7519 (2020)
9. Zhao, L., Li, H., Wu, X., Zhang, J.: An improved phase-shifted full-bridge converter with wide-range ZVS and reduced filter requirement. IEEE Trans. Ind. Electron. 65(3), 2167–2176 (2018)

10. Teng, J., Liu, B.: Three-stage dead-time adjustment scheme for conversion efficiency enhancement of phase-shift full-bridge converters at light loads. IEEE Trans. Ind. Electron. 68(2), 1210–1219 (2021)

11. Shih, L., Liu, Y., Chiu, H.: A novel hybrid mode control for a phase-shift full-bridge converter featuring high efficiency over a full-load range. IEEE Trans. Power Electron. 34(3), 2794–2804 (2019)

12. Lim, J., Hassan, J., Kim, M.: Bidirectional soft switching push–pull resonant converter over wide range of battery voltages. IEEE Trans. Power Electron. 36(11), 12251–12267 (2021)

13. Das, D., Weise, N., Basu, K., Baranwal, R., Mohan, N.: A bidirectional soft-switched DAB-based single-stage three-phase AC–DC converter for V2G application. IEEE Trans. Transp. Electrif. 5(1), 186–199 (2019)

14. Shahabi, A., Lemmon, A., Graves, R., Banerjee, S., Gant, L., Jenkins, L.L.: A SiC-based isolated DC/DC converter for high density data center applications. In: *2018 IEEE Applied Power Electronics Conference and Exposition (APEC)*, San Antonio, TX, USA, pp. 2294–2301 (2018) https://doi.org/10.1109/APEC.2018.8341336.

15. Shah, S.S., Rastogi, S.K., Bhattacharya, S.: Paralleling of LLC resonant converters. IEEE Trans. Power Electron. 36(6), 6276–6287 (2021)

16. Wei, Y., Luo, Q., Mantooth, A.: Overview of modulation strategies for LLC resonant converter. IEEE Trans. Power Electron. 35(10), 10423–10443 (2020)

17. Tian, S., Lee, F.C., Li, Q.: Equivalent circuit modeling of LLC resonant converter. IEEE Trans. Power Electron. 35(8), 8833–8845 (2020)

18. Shen, Y., Zhao, W., Chen, Z., Cai, C.: Full-bridge LLC resonant converter with series-parallel connected transformers for electric vehicle on-board charger. IEEE Access 6, 13490–13500 (2018)

19. Chunxue, W., Mingming, H., Changbin, H., Zhengguo, P., Jinghua, Z.: Research on characteristics of bidirectional CLLC DC–DC transformer used in DC microgrid. J. Eng. 2019(18), 5351–5354 (2019).

20. Min, J., Ordonez, M.: Bidirectional resonant CLLC charger for wide battery voltage range: Asymmetric parameters methodology. IEEE Trans. Power Electron. 36(6), 6662–6673 (2021)

21. Huang, J., Zhang, X., Zhao, B.: Simplified resonant parameter design of the asymmetrical CLLC-type DC transformer in the renewable energy system via semi-artificial intelligent optimal scheme. IEEE Trans. Power Electron. 35(2), 1548–1562 (2020)

22. Huang, J. et al.: Robust circuit parameters design for the CLLC-Type DC transformer in the hybrid AC–DC microgrid. IEEE Trans. Ind. Electron. 66(3), 1906–1918 (2019)

23. Li, X., Huang, J., Ma, Y., Wang, X., Yang, J., Wu, X.: Unified modeling, analysis, and design of isolated bidirectional CLLC resonant DC–DC converters. IEEE J. Emerging Sel. Top. Power Electron. 10(2), 2305–2318 (2022)

24. Zou, S., Lu, J., Mallik, A., Khaligh, A.: Bi-directional CLLC converter with synchronous rectification for plug-in electric vehicles. IEEE Trans. Ind. Appl. 54(2), 998–1005 (2018)

25. Sankar, A., Mallik, A., Khaligh, A.: Extended harmonics based phase tracking for synchronous rectification in CLLC converters. IEEE Trans. Ind. Electron. 66(8), 6592–6603 (2019)

26. Dalala, Z.M., Zahid, Z.U., Saadeh, O.S., Lai, J.-S.: Modeling and controller design of a bidirectional resonant converter battery charger. IEEE Access 6, 23338–23350 (2018)

27. Song, J.Q., Yang, D.J., Zhang, C.H., Duan, B.: Hybrid control method for CLLLC resonant converter with Low output voltage ripple. IFAC-PapersOnLine 51(31), 680–684 (2018)

28. Deng, Q., He, Y., Lei, C., Liu, J.: Research on CLLLC bi-directional resonant based on time-domain analysis. In: *2020 IEEE 3rd Student Conference on Electrical Machines and Systems*, Jinan, China, pp. 724–729 (2020), https://doi.org/10.1109/SCEMS48876.2020.9352422.

29. Li, K., Wang, Y., Xu, J.H.; Gao, G.Q., Xu, P.F., Li, T., Zhang, X.J.: Modeling and hybrid controller design of CLLLC. In: *2019 IEEE 10th International Symposium on Power Electronics for Distributed Generation Systems (PEDG)*, Xi'an, China, pp. 168–172 (2019), https://doi.org/10.1109/PEDG.2019.8807509.

30. Yudi, X., Xingkui, M., Zhe, Z., Shi, Y.: New hybrid control for wide input full-bridge LLC resonant DC/DC converter. In: *2018 3rd International Conference on Intelligent Green Building and Smart Grid (IGBSG)*, Yilan, Taiwan, pp. 1–4 (2018) https://doi.org/10.1109/IGBSG.2018.8393556.

31. Wolfspeed, "1200V Discrete Silicon Carbide MOSFETs," C2M0160120D datasheet, (2020). https://assets.wolfspeed.com/uploads/2020/12/C2M0160120D.pdf

32. Unitedsic, "SIC FETs/UJ3C SiC FET Series," UJ3C065080K3S datasheet, (2017). https://unitedsic.com/datasheets/DS_UJ3C065080K3S.pdf